13th International Symposium on Turbulence and Shear Flow Phenomena (TSFP13)
Montreal, Canada, June 25–28, 2024

SPARSE SENSOR PLACEMENT FOR TURBULENT FLOW FIELD RECONSTRUCTION BASED ON MEAN-FLOW-LINEARIZED DYNAMICS

Benjamin Herrmann
Department of Mechanical Engineering
University of Chile
Beauchef 851, Santiago, Chile
benjaminh@uchile.cl

Erick Kracht
Department of Mechanical Engineering
University of Chile
Beauchef 851, Santiago, Chile
erick.kracht@gmail.com

Steven L. Brunton
Department of Mechanical Engineering
University of Washington
Seattle, WA 98195, USA
sbrunton@uw.edu

Beverley J. McKeon
Department of Mechanical Engineering
Stanford University
Stanford, CA 94305, USA
bjmckeon@stanford.edu

ABSTRACT

Data-driven methods are improving our capability to predict, control and understand turbulent flows. However, these techniques often rely on having access to complete flow field measurements, which are difficult to acquire due to the multi-scale nature of turbulence. Fortunately, velocity field data may be reconstructed from measurements of a few "strategically placed" point sensors. In recent work, we achieved this by combining a greedy sensor selection algorithm with a low-rank representation of the flow in terms of the leading empirical orthogonal functions (EOFs) that arise from the mean flow linearization (Herrmann *et al.*, 2023). Here, we include an eddy viscosity model in our linearized equations to compute eddy EOFs to investigate if they offer a more efficient low-rank representation for coherent perturbations of the mean flow. We test our method on data from numerical simulations of turbulent flow in a minimal channel at $\mathrm{Re}_\tau = 185$. The flow reconstruction performance and sensor locations are investigated and compared with those obtained using a data-driven sensor placement strategy based on proper orthogonal decomposition modes. Our equation-based framework proves to be an attractive alternative, since it performs similarly to the data-driven approach, but it does not require data snapshots and relies only on knowledge of the mean flow.

INTRODUCTION

Reconstruction of velocity fluctuations from sparse sensor measurements remains an open challenge due to the complexity of high-dimensional turbulence (Arun *et al.*, 2023). Such a reconstruction would enable the use of emerging data-driven methods — which require complete flow field snapshot data — to build reduced-order models that are useful to predict, control, and understand the dominant underlying flow physics (Taira *et al.*, 2017; Brunton *et al.*, 2020; Herrmann *et al.*, 2021; Schmid, 2022; Baddoo *et al.*, 2022, 2023).

Recently, Towne *et al.* (2020) formulated a resolvent-based method to estimate space-time flow statistics from limited data. Subsequently, Martini *et al.* (2020) and Amaral *et al.* (2021) developed and applied, respectively, an optimal and noncausal resolvent-based estimator that is able to reconstruct unmeasured, time-varying, flow quantities from limited experimental data as post-processing. Arun *et al.* (2023) developed a framework for efficient streaming reconstructions of turbulent velocity fluctuations from sparse sensor measurements aimed at real-time applications.

More recently, Herrmann *et al.* (2023) proposed and demonstrated a framework for sparse sensor placement for reconstruction of turbulent channel flow. The approach uses a greedy algorithm for scalable sensor selection (Manohar *et al.*, 2018), and leverages a low-rank representation of the flow field in terms of modes arising from the mean-flow-linearized Navier–Stokes operator. Specifically, the leading eigenvectors of the controllability Gramian are used as a basis. These modes, also known as empirical orthogonal functions (EOFs), represent the flow structures that account for most of the sustained variance in the response to delta-correlated white-noise forcing (Farrell & Ioannou, 1993; Dergham *et al.*, 2013). Moreover, EOFs enjoy a well-established connection to resolvent response modes (Zhou *et al.*, 1999; Farrell & Ioannou, 2001; Dergham *et al.*, 2011). In this work, we include an eddy viscosity model in the mean-flow-linearization to obtain eddy EOFs in search for a more efficient low-rank representation of coherent perturbations in wall-bounded turbulent flows. With these modes, we investigate whether we can improve the performance of our method to reconstruct turbulent flows from sparse sensor data (Herrmann *et al.*, 2023).

Sparse sensor placement for reconstruction

Consider sparse observations $\boldsymbol{y} = \boldsymbol{P}^{\mathrm{T}}\boldsymbol{x}$ of the state $\boldsymbol{x} \in \mathbb{R}^n$ of a dynamical system, where $\boldsymbol{P} = [\boldsymbol{e}_{\gamma_1} \; \cdots \; \boldsymbol{e}_{\gamma_r}] \in \mathbb{R}^{n\times r}$ is a sampling matrix containing r columns of the identity matrix. Reconstruction of $\boldsymbol{x}$ from $\boldsymbol{y}$ can be achieved by using a low-rank representation of the state $\boldsymbol{a} \in \mathbb{R}^r$, given by a basis $\boldsymbol{V} \in \mathbb{R}^{n\times r}$ so that $\boldsymbol{x} \approx \boldsymbol{V}\boldsymbol{a} \Rightarrow \boldsymbol{y} \approx \boldsymbol{P}^{\mathrm{T}}\boldsymbol{V}\boldsymbol{a}$, and solving in the least squares sense to obtain $\boldsymbol{a} = (\boldsymbol{P}^{\mathrm{T}}\boldsymbol{V})^{-1}\boldsymbol{y}$. The problem of sensor selection for state reconstruction amounts to designing $\boldsymbol{P}$ so that the matrix $\boldsymbol{P}^{\mathrm{T}}\boldsymbol{V}$ is well conditioned for inversion, producing an approximation of $\boldsymbol{x}$ that can be robustly inferred from $\boldsymbol{y}$ (Manohar

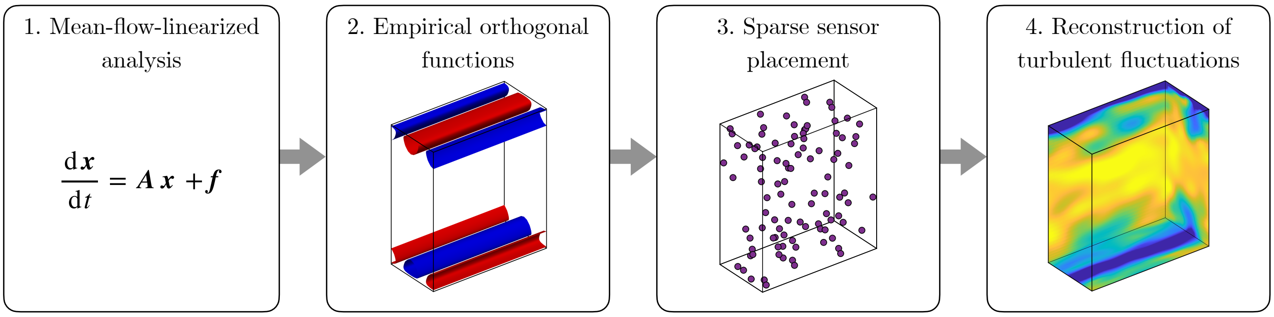

Figure 1. Schematic of the proposed method. Modes from mean-flow-linearized analysis are used together with greedy sensor placement strategies to reconstruct turbulent velocity fluctuations from sparse measurements.

et al., 2018). The resulting reconstruction $\tilde{\boldsymbol{x}}$ can be interpreted as an interpolatory projection of the true state onto the span of $\boldsymbol{V}$ using the interpolation points selected by $\boldsymbol{P}$, as follows

$$\tilde{\boldsymbol{x}} = \boldsymbol{V}(\boldsymbol{P}^{\mathrm{T}}\boldsymbol{V})^{-1}\boldsymbol{y} = \boldsymbol{V}(\boldsymbol{P}^{\mathrm{T}}\boldsymbol{V})^{-1}\boldsymbol{P}^{\mathrm{T}}\boldsymbol{x} = \mathbb{P}\boldsymbol{x}, \tag{1}$$

with $\mathbb{P}$ being the interpolatory projector (Sorensen & Embree, 2016; Herrmann *et al.*, 2023).

Finding the optimal sampling matrix that minimizes the projection error for a given basis $\boldsymbol{V}$ requires a brute force search over all possible sampling location combinations. While this can be achieved for small-scale systems (Chen & Rowley, 2011), with $n \sim O(10^4)$ at the moment of this writing, the computational cost makes it intractable in higher dimensions. Alternatively, there are several fast greedy algorithms that can be used to approximate the optimal sensor locations avoiding the combinatorial search. In the context of reduced-order modeling, the empirical and discrete empirical interpolation methods, EIM (Barrault *et al.*, 2004) and DEIM (Chaturantabut & Sorensen, 2010), were developed to find locations to interpolate nonlinear terms in a high-dimensional dynamical system, which is known as hyper-reduction. An even simpler and equally efficient approach is the Q-DEIM algorithm, introduced by Drmac & Gugercin (2016), which leverages the pivoted QR factorization to select the sampling points. Manohar *et al.* (2018) showed that this is also a robust strategy for sparse sensor placement for state reconstruction in a variety of applications.

METHODOLOGY

This section describes our approach for sensor selection informed by the mean-flow-linearized dynamics, the numerical setup for the simulations carried out to test the method, and the computation of the modes used as bases for the interpolatory projections.

Equation-based sparse sensor placement

In the context of this work, the state $\boldsymbol{x}$ corresponds to a spatial discretization of velocity fluctuations in a turbulent flow. The evolution of these fluctuations is governed by

$$\frac{\mathrm{d}\boldsymbol{x}}{\mathrm{d}t} = \boldsymbol{A}\boldsymbol{x} + \boldsymbol{f}, \tag{2}$$

where $\boldsymbol{A} \in \mathbb{R}^{n\times n}$ is the mean flow linearization operator (with or without an eddy viscosity model) and $\boldsymbol{f} \in \mathbb{R}^n$ is the forcing containing the nonlinear terms McKeon & Sharma (2010). The incompressible Navier–Stokes equations can be written in this form by projecting the velocity field onto a divergence-free basis to eliminate the pressure variable.

The quality of the state reconstruction from sparse sensors, given by (1), depends strongly on both the low-rank representation, given by the basis $\boldsymbol{V}$, and the sensor placement, given by the sampling matrix $\boldsymbol{P}$. In the context of fluid flows, $\boldsymbol{V}$ may be formed using a variety of data-driven or equation-based modal decompositions (Taira *et al.*, 2017). In this work, we opt for an equation-based approach and take the leading empirical orthogonal functions (EOFs) as our modes (Herrmann *et al.*, 2023). The EOFs represent the flow structures that account for most of the sustained variance in the response to delta-correlated white noise forcing (Farrell & Ioannou, 1993, 2001; Dergham *et al.*, 2013), and can be computed as the leading eigenvectors of the full-input controllability Gramian, given by

$$\boldsymbol{W_c} = \int_0^\infty e^{\boldsymbol{A}t} e^{\boldsymbol{A}^* t}\,\mathrm{d}t = \frac{1}{2\pi}\int_{-\infty}^{\infty} \boldsymbol{H}(i\omega)\boldsymbol{H}^*(i\omega)\,\mathrm{d}\omega, \tag{3}$$

where $\boldsymbol{A}$ is the mean flow linearization operator, $e^{\boldsymbol{A}t}$ is the time propagator, and $\boldsymbol{H}(i\omega)$ is the resolvent operator. Alternatively, EOFs admit deterministic interpretations as the solutions to the optimization problems

$$\boldsymbol{v} = \underset{\boldsymbol{v}}{\mathrm{argmax}} \frac{\|e^{\boldsymbol{A}^* t}\boldsymbol{v}\|^2_{\mathcal{L}_2}}{\|\boldsymbol{v}\|^2} = \underset{\boldsymbol{v}}{\mathrm{argmax}} \frac{\|\boldsymbol{H}(i\omega)^*\boldsymbol{v}\|^2_{\mathcal{L}_2}}{\|\boldsymbol{v}\|^2}, \tag{4}$$

where the $\mathcal{L}_2$−norm represents energy integrated over time or across all frequencies. Therefore, the leading EOFs represent the flow structures that best align with the optimal responses to initial conditions over all time horizons and, equivalently, to the optimal responses to harmonic forcings across all frequencies. In this work we consider the cases with and without an eddy viscosity model and therefore compute EOFs and eddy EOFs.

Once the basis is determined, the sensor placement problem can be solved using one of several available greedy algorithms to avoid the brute-force search over all possible sampling locations, such as the discrete empirical interpolation method (DEIM) (Chaturantabut & Sorensen, 2010) or QR-pivoting (Drmac & Gugercin, 2016; Manohar *et al.*, 2018). Here, we adhere to the latter method because it provides near-optimal interpolation points and is simple to implement leveraging the pivoted QR factorization available in most scientific computing software packages. A schematic of the proposed approach is shown in figure 1.

Direct numerical simulations

As a test bed system, we use a minimal channel flow at $\mathrm{Re}_\tau = 185$. This corresponds to a pressure-driven turbu-

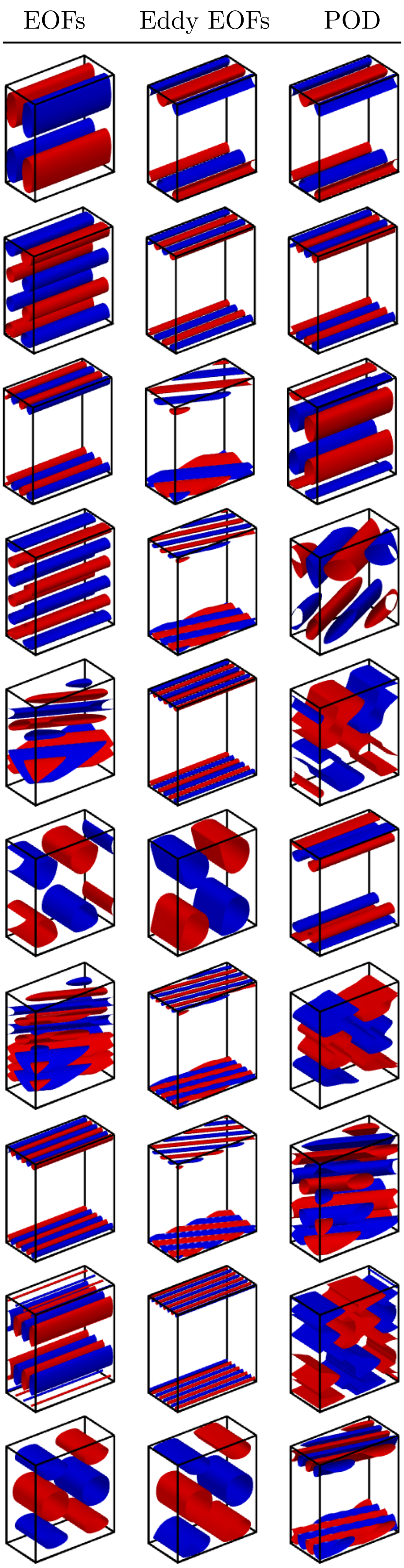

Figure 2. Isosurfaces of streamwise velocity for the leading EOFs, eddy EOFs and POD modes for turbulent channel flow. Symmetry-related modes and mean flow modes are skipped to show a larger variety of structures.

lent flow, governed by the incompressible Navier–Stokes equations, in a doubly-periodic plane channel. The domain size is $1.83 \times 2 \times 0.92$ dimensionless length units along the x, y, and z coordinates that indicate the streamwise (periodic), wall-normal, and spanwise (periodic) directions, respectively. For a Reynolds number of $\mathrm{Re} = 4200$, based on the channel half-height h and the centerline velocity for the laminar parabolic profile $U_{c,\mathrm{lam}}$, leading to $\mathrm{Re}_\tau = 185$, this is the smallest domain that is able to sustain turbulence and is known as a minimal flow unit (Jiménez & Moin, 1991).

We use the spectral code *Channelflow* (Gibson *et al.*, 2008; Gibson, 2014) to perform direct numerical simulations (DNS) and generate a dataset comprised of a long sequence of snapshots acquired after statistically stationarity is reached. The code uses Chebyshev and Fourier expansions of the flow field in the wall-normal and horizontal directions, and a 3^{rd}-order Adams–Bashforth backward differentiation scheme for the time integration. We find that a grid with $32 \times 101 \times 16$ (after de-aliasing) in x, y, and z and a time step of 0.005 time units are sufficient to discretize the domain and keep the CFL number below 0.55, for the case studied. The flow is initialized from a random perturbation of the laminar profile, simulated for 10^4 time units (based on $h/U_{c,\mathrm{lam}}$) until transients have died out and statistical stationarity is reached, and then velocity field snapshots are saved every 0.2 time units for over an additional 1.5×10^4 time units, which is enough to get converged statistics. The streamwise velocity for a typical flow field snapshot is shown in figure 3(*b*).

Modal bases

Proper orthogonal decomposition (POD) modes are computed from the DNS dataset. First, the snapshots are Fourier-transformed in the horizontal directions and an independent analysis is carried out for each pair of streamwise and spanwise wavenumbers. This ensures that the resulting modes respect the shift-equivariance of the flow in the homogeneous directions (Sirovich, 1987). Moreover, flow through a plane channel is also equivariant under the dihedral group of transformations D_2, meaning that, a vertical reflection, a spanwise reflection, or a rotation about the x-axis of an observed flow field yields another admissible flow field (Sirovich, 1987). To respect these symmetries, the appropriate transformations are applied to the Fourier-transformed flow fields and appended as additional data snapshots before proceeding with the decomposition.

Furthermore, EOFs and eddy EOFs are computed from the mean-flow-linearized governing equations. The mean flow is computed from the DNS snapshots and used to build the mean-flow-linearized operators with an in-house code based on the modified Orr–Sommerfeld/Squire formulation to account for spatial variations of viscosity in the wall-normal direction as in (Reynolds & Hussain, 1972; Del Alamo & Jimenez, 2006; Pujals *et al.*, 2009; Hwang & Cossu, 2010*b*,*a*; Morra *et al.*, 2019; Symon *et al.*, 2023). Moreover, for zero streamwise and spanwise wavenumbers, we replace the Orr–Sommerfeld/Squire operator for the viscous diffusion operator acting on the wall-normal and streamwise velocities, as in earlier works (Waleffe, 1997; Cavalieri & Nogueira, 2022). Our code uses Chebyshev spectral collocation to discretize the wall-normal direction with the same grid used in the DNS. For the eddy viscosity, we use the Cess profile (Cess, 1958)

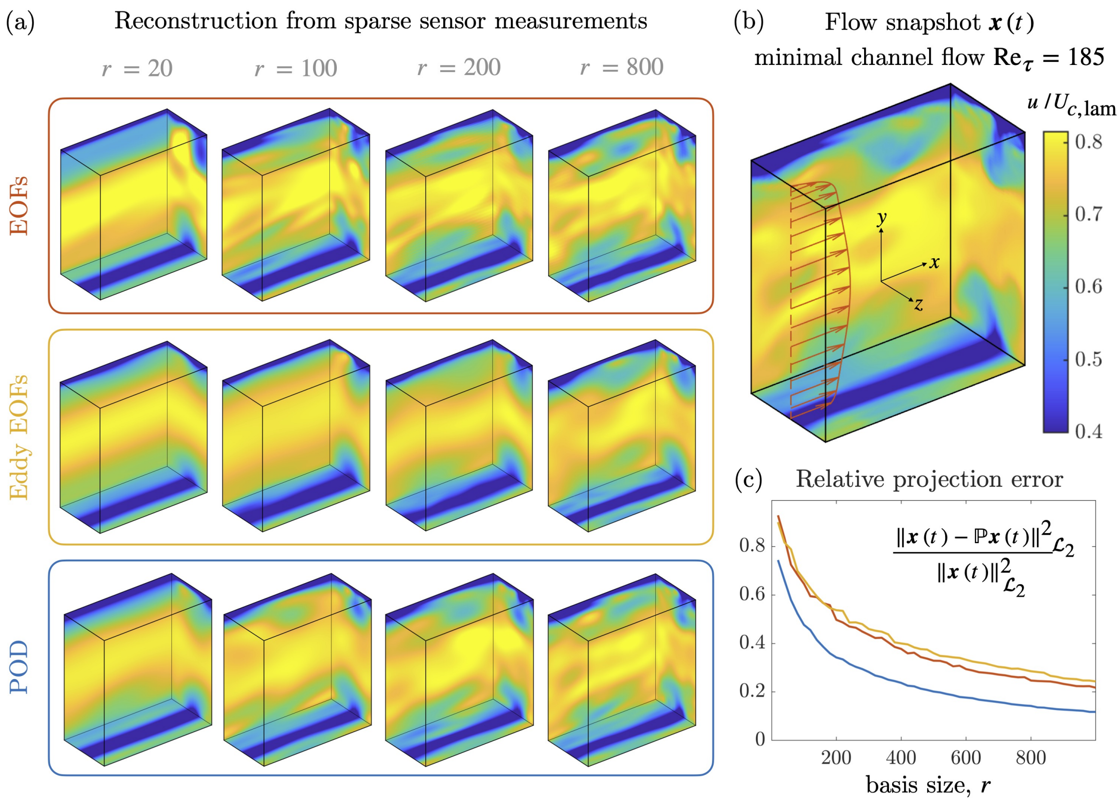

Figure 3. Sparse sensor placement for reconstruction of velocity fluctuations in the turbulent flow in a minimal channel at $\mathrm{Re}_\tau = 185$. (*a*) Reconstructed snapshots based on r sparse sensor measurements and EOFs (red), eddy EOFs (yellow), and POD modes (blue). (*b*) The flow field snapshot from the DNS being reconstructed. The colormap shows streamwise velocity. (*c*) Normalized reconstruction error in the $\mathcal{L}_2$-norm as a function of basis size using the three bases.

$$\nu_T(y) = \frac{1}{2\mathrm{Re}_\tau}\left(\left[1 + \frac{\kappa^2\mathrm{Re}_\tau^2}{9}(1-y^2)^2(1+2y^2)^2\right.\right.$$
$$\left.\left.\left(1-\exp\left[(|y|-1)\frac{\mathrm{Re}_\tau}{A}\right]\right)^2\right]^{1/2}+1\right), \qquad (5)$$

where the constants $\kappa = 0.426$ and $A = 25.4$ were selected to fit experimental mean velocity profiles at $\mathrm{Re}_\tau = 2000$ by Del Alamo & Jimenez (2006). In equation (5), $\nu_T(y)$ represents the total effective viscosity that has been made nondimensional using the scale $u_\tau h$ based on the friction velocity and the channel half-height. Therefore, in the nondimensional linearized equations, we either use $1/\mathrm{Re}_\tau$ in front of the viscous terms to consider only the molecular viscosity, or replace it by ν_T to incorporate the eddy viscosity model. The Fourier-transformed (in the homogeneous directions) linearized operators with and without eddy viscosity are built for every wavenumber tuple in the range resolved by the DNS. The controllability Gramians, considering full state inputs, are computed by solving the corresponding Lyapunov equation with available routines in Matlab. EOFs and eddy EOFs are obtained as the eigenvectors of the respective controllability Gramian.

For each basis, the modes obtained for all wavenumbers are stacked together and sorted in descending order according to their energy content, that is, the singular values of the data matrix for the POD modes, and the eigenvalues of the controllability Gramians for the EOFs and eddy EOFs. Finally, an inverse Fourier transform is applied to take the three sets of modes to physical coordinates. The leading flow structures corresponding to each basis are shown in figure 2. Interpolatory projections of velocity fluctuation snapshots from the DNS are investigated. The EOFs, arising from the mean flow-linearization with and without an eddy viscosity model, and POD modes are compared as bases for the projections.

RESULTS AND DISCUSSION

We assess the performance of the presented framework to reconstruct velocity fluctuations in the minimal channel flow from sparse sensor measurements, as shown in figure 3. To assess the performance, our metric of choice is the normalized $\mathcal{L}_2$−norm of the state reconstruction error computed over the entire dataset. Under this metric, POD modes provide the optimal low-rank approximation of the state. Therefore, the reconstruction error obtained using POD serves as a lower bound for our data-free approach that leverages the EOFs and eddy EOFs.

Considering the leading r elements in each basis, we build interpolatory projectors using r tailored sensors, selected using pivoted QR, that are complemented with an additional $2r$ random sensors. Because this is a high-dimensional system with a total of $n \approx 1.6 \cdot 10^5$ states, complementing tailored sensors with random ones is a simple strategy to improve the resulting reconstruction that was suggested in the work of Manohar *et al.* (2018). This is implemented by simply taking the leading $2r$ columns of a matrix containing all remaining possible sensors after a random column permutation. These columns are then concatenated to the sampling matrix P used to build the projector. Increasing r improves the reconstruction performance with diminishing returns, quickly at first and slower for a larger basis size, as shown in figure 3(*c*). Importantly, the reconstruction error using the equation-based approach with EOFs or eddy

Wavevector direction	EOFs	Eddy EOFs	POD
Streamwise	118	124	122
Spanwise	116	76	164
Oblique	744	780	687
Mean flow mode	22	20	27

Table 1. Classification of the leading 1000 EOFs, eddy EOFs, and POD modes according to their wavevector direction.

EOFs follow closely that obtained with the POD modes.

Leveraging the EOFs and eddy EOFs, the reconstruction explains a large portion of the variance in the flow field, capturing 50% of the kinetic energy of the turbulent fluctuations with around 200 modes and 600 sensors, and more than 75% with 1000 modes and 3000, which amounts to measuring less than 2% of the full state. Here, we expected to find an improvement in the reconstruction performance by using eddy EOFs over that of using EOFs, due to the eddy viscosity partially accounting for the colored statistics of the nonlinear forcing. However, our results show that the reconstruction error obtained with both approaches is very similar and, interestingly, the performance including an eddy viscosity model is slightly worse.

Motivated by this finding, we take a more detailed look into the spatial structure of the EOFs, eddy EOFs, and POD modes, and their capability to capture the DNS data. First, we analyze the types of flow structures contained in each basis by counting, within the first 1000 modes, how many of them correspond to streamwise, spanwise, or oblique waves or to mean flow modes. This classification, shown in table 1, reveals that, compared to the POD basis, both EOFs and eddy EOFs include a significantly larger amount of oblique waves in place of missing spanwise waves (streamwise streaks). This is more pronounced for the basis of eddy EOFs, which contains less than half the amount of streamwise streak modes, within the leading 1000 modes, than the POD basis does.

In addition, we examine the spatial support of the combination of modes within each basis. For this purpose, we compute the orthogonal projection of the DNS data onto the leading 1000 EOFs, eddy EOFs, and POD modes. We then compute the wall-normal distribution of the RMS of the projection error as follows

$$\boldsymbol{e}(y) = (e_u, e_v, e_w)^{\mathrm{T}} = \frac{1}{TL_zL_x}\int_0^T\int_0^{L_z}\int_0^{L_x} |\boldsymbol{x}-\tilde{\boldsymbol{x}}|^2 \mathrm{d}x\mathrm{d}z\mathrm{d}t, \quad (6)$$

where $\boldsymbol{x}$ is the fluctuation velocity field from the DNS and $\tilde{\boldsymbol{x}} = \boldsymbol{V}\boldsymbol{V}^{\mathrm{T}}\boldsymbol{x}$ is its orthogonal projection onto the corresponding basis $\boldsymbol{V}$. This error metric is plotted for the three velocity components in figure 4. We find that, compared to the projection onto eddy EOFs, the projection onto EOFs results in a lower error almost everywhere. Nevertheless, for the eddy EOFs, there is a big dip in the error distribution for the streamwise component in the buffer layer at the location corresponding to the peak RMS for the streamwise velocity fluctuations. In addition, eddy EOFs also do a better job than EOFs at capturing the wall-normal velocity fluctuations in the logarithmic layer. However, these localized performance advantages of the eddy EOFs do not compensate for the EOFs better capturing the flow field in the viscous sublayer and, most notably, towards channel center where the latter perform almost as well as POD modes. These results are in agreement with the recent work of Symon *et al.* (2023), who found that eddy resolvent modes were better aligned with SPOD modes than standard resolvent modes for flow structures associated with the near-wall cycle.

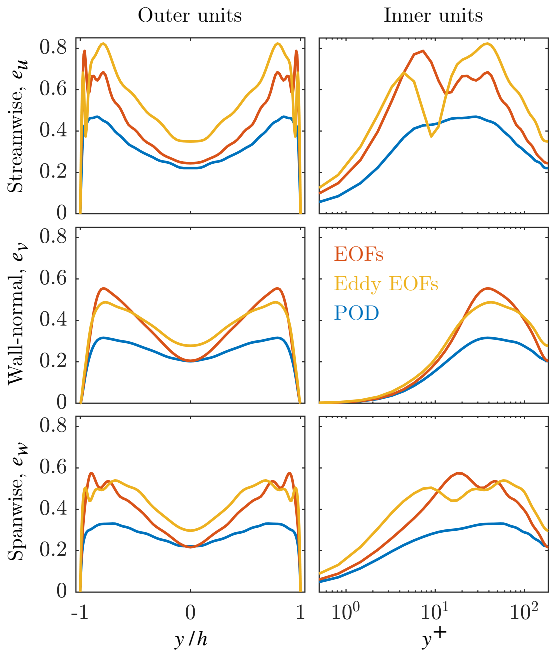

Figure 4. Wall-normal distribution of the RMS of the orthogonal projection error obtained using the leading 1000 EOFs, eddy EOFs, and POD modes as bases. Error metric defined in eq. (6)

CONCLUSIONS

The EOFs provide an orthonormal basis of flow structures that are hierarchically ordered by their accounting of the flow response to forcing. In fact, they provide a basis that is optimal for state reconstruction in the case of white-noise forcing. Furthermore, these modes coincide with POD modes for a stable linear system where every state is disturbed (Rowley, 2005). However, for turbulent flows, the EOFs of the mean-flow linearization form a sub-optimal basis for state reconstruction because of the colored forcing statistics. Moreover, rather than accounting for this effect, incorporating an eddy viscosity model produces eddy EOFs that perform slightly worse than standard EOFs at reconstructing turbulent fluctuations. Nevertheless, eddy EOFs are found to better represent streamwise and spanwise velocity structures in the buffer layer and wall-normal velocity structures in the logarithmic layer. Further differences between the flow structures produced by the different modal analyses should be investigated in future work. Furthermore, obtaining converged POD modes requires long data sequences, whereas the EOFs (or eddy EOFs) require only knowledge of the mean flow. This is particularly appealing for the case of turbulent flows, where fully space- and time-resolved velocity field data snapshots can be obtained only numerically, whereas the mean flow can be obtained from experiments. Importantly, we showed that, for a minimal channel flow, the state reconstruction performance of the EOFs and eddy EOFs follow closely that of POD, even though this is achieved without any data snapshots. Therefore, for turbulent flows, the presented approach based on EOFs of the mean flow linearization and QR-pivoting is an attractive equation-based alternative to the POD-based data-driven framework introduced by Manohar *et al.* (2018).

REFERENCES

Amaral, Filipe R, Cavalieri, André VG, Martini, Eduardo, Jordan, Peter & Towne, Aaron 2021 Resolvent-based estimation of turbulent channel flow using wall measurements. *Journal of Fluid Mechanics* **927**, A17.

Arun, Rahul, Bae, H Jane & McKeon, Beverley J 2023 Towards real-time reconstruction of velocity fluctuations in turbulent channel flow. *Physical Review Fluids* **8** (6), 064612.

Baddoo, Peter J, Herrmann, Benjamin, McKeon, Beverley J & Brunton, Steven L 2022 Kernel learning for robust dynamic mode decomposition: linear and nonlinear disambiguation optimization. *Proceedings of the Royal Society A* **478** (2260), 20210830.

Baddoo, Peter J, Herrmann, Benjamin, McKeon, Beverley J, Nathan Kutz, J & Brunton, Steven L 2023 Physics-informed dynamic mode decomposition. *Proceedings of the Royal Society A* **479** (2271), 20220576.

Barrault, Maxime, Maday, Yvon, Nguyen, Ngoc Cuong & Patera, Anthony T 2004 An empirical interpolation method: application to efficient reduced-basis discretization of partial differential equations. *Comptes Rendus Mathematique* **339** (9), 667–672.

Brunton, Steven L, Noack, Bernd R & Koumoutsakos, Petros 2020 Machine learning for fluid mechanics. *Annual Review of Fluid Mechanics* **52**, 477–508.

Cavalieri, André VG & Nogueira, Petrônio AS 2022 Reduced-order Galerkin models of plane Couette flow. *Physical Review Fluids* **7** (10), L102601.

Cess, RD 1958 A survey of the literature on heat transfer in turbulent tube flow. *Res. Rep* pp. 8–0529.

Chaturantabut, Saifon & Sorensen, Danny C 2010 Nonlinear model reduction via discrete empirical interpolation. *SIAM Journal on Scientific Computing* **32** (5), 2737–2764.

Chen, Kevin K & Rowley, Clarence W 2011 H_2 optimal actuator and sensor placement in the linearised complex Ginzburg-Landau system. *Journal of Fluid Mechanics* **681**, 241–260.

Del Alamo, Juan C & Jimenez, Javier 2006 Linear energy amplification in turbulent channels. *Journal of Fluid Mechanics* **559**, 205–213.

Dergham, G, Sipp, D & Robinet, J-C 2011 Accurate low dimensional models for deterministic fluid systems driven by uncertain forcing. *Physics of Fluids* **23** (9), 094101.

Dergham, G, Sipp, D & Robinet, J-Ch 2013 Stochastic dynamics and model reduction of amplifier flows: the backward facing step flow. *Journal of Fluid Mechanics* **719**, 406–430.

Drmac, Zlatko & Gugercin, Serkan 2016 A new selection operator for the discrete empirical interpolation method—improved a priori error bound and extensions. *SIAM Journal on Scientific Computing* **38** (2), A631–A648.

Farrell, Brian F & Ioannou, Petros J 1993 Stochastic forcing of the linearized navier–stokes equations. *Physics of Fluids A: Fluid Dynamics* **5** (11), 2600–2609.

Farrell, Brian F & Ioannou, Petros J 2001 Accurate low-dimensional approximation of the linear dynamics of fluid flow. *Journal of the Atmospheric Sciences* **58** (18), 2771–2789.

Gibson, J. F. 2014 Channelflow: A spectral Navier-Stokes simulator in C++. *Tech. Rep.*. U. New Hampshire.

Gibson, John F, Halcrow, Jonathan & Cvitanović, Predrag 2008 Visualizing the geometry of state space in plane Couette flow. *Journal of Fluid Mechanics* **611**, 107–130.

Herrmann, Benjamin, Baddoo, Peter J., Dawson, Scott T.M., Semaan, Richard, Brunton, Steven L. & McKeon, Beverley J. 2023 Interpolatory input and output projections for flow control. *Journal of Fluid Mechanics* **971**, A27.

Herrmann, Benjamin, Baddoo, Peter J, Semaan, Richard, Brunton, Steven L & McKeon, Beverley J 2021 Data-driven resolvent analysis. *Journal of Fluid Mechanics* **918**, A10.

Hwang, Yongyun & Cossu, Carlo 2010*a* Amplification of coherent streaks in the turbulent Couette flow: an input–output analysis at low Reynolds number. *Journal of Fluid Mechanics* **643**, 333–348.

Hwang, Yongyun & Cossu, Carlo 2010*b* Linear non-normal energy amplification of harmonic and stochastic forcing in turbulent channel flow. *Journal of Fluid Mechanics* **664**, 51–73.

Jiménez, Javier & Moin, Parviz 1991 The minimal flow unit in near-wall turbulence. *Journal of Fluid Mechanics* **225**, 213–240.

Manohar, Krithika, Brunton, Bingni W, Kutz, J Nathan & Brunton, Steven L 2018 Data-driven sparse sensor placement for reconstruction: Demonstrating the benefits of exploiting known patterns. *IEEE Control Systems Magazine* **38** (3), 63–86.

Martini, Eduardo, Cavalieri, André VG, Jordan, Peter, Towne, Aaron & Lesshafft, Lutz 2020 Resolvent-based optimal estimation of transitional and turbulent flows. *Journal of Fluid Mechanics* **900**, A2.

McKeon, Beverley J. & Sharma, Ati S. 2010 A critical-layer framework for turbulent pipe flow. *Journal of Fluid Mechanics* **658**, 336–382.

Morra, Pierluigi, Semeraro, Onofrio, Henningson, Dan S & Cossu, Carlo 2019 On the relevance of reynolds stresses in resolvent analyses of turbulent wall-bounded flows. *Journal of Fluid Mechanics* **867**, 969–984.

Pujals, Gregory, García-Villalba, Manuel, Cossu, Carlo & Depardon, Sebastien 2009 A note on optimal transient growth in turbulent channel flows. *Physics of fluids* **21** (1).

Reynolds, WC & Hussain, AKMF 1972 The mechanics of an organized wave in turbulent shear flow. part 3. theoretical models and comparisons with experiments. *Journal of Fluid Mechanics* **54** (2), 263–288.

Rowley, C. W. 2005 Model reduction for fluids, using balanced proper orthogonal decomposition. *International Journal of Bifurcation and Chaos* **15**, 997–1013.

Schmid, Peter J 2022 Dynamic mode decomposition and its variants. *Annual Review of Fluid Mechanics* **54**, 225–254.

Sirovich, Lawrence 1987 Turbulence and the dynamics of coherent structures. II. Symmetries and transformations. *Quarterly of Applied Mathematics* **45** (3), 573–582.

Sorensen, Danny C & Embree, Mark 2016 A DEIM induced CUR factorization. *SIAM Journal on Scientific Computing* **38** (3), A1454–A1482.

Symon, Sean, Madhusudanan, Anagha, Illingworth, Simon J & Marusic, Ivan 2023 Use of eddy viscosity in resolvent analysis of turbulent channel flow. *Physical Review Fluids* **8** (6), 064601.

Taira, Kunihiko, Brunton, Steven L, Dawson, Scott T M, Rowley, Clarence W, Colonius, Tim, McKeon, Beverley J, Schmidt, Oliver T, Gordeyev, Stanislav, Theofilis, Vassilios & Ukeiley, Lawrence S 2017 Modal analysis of fluid flows: An overview. *AIAA Journal* **55** (12), 4013–4041.

Towne, Aaron, Lozano-Durán, Adrián & Yang, Xiang 2020 Resolvent-based estimation of space–time flow statistics. *Journal of Fluid Mechanics* **883**, A17.

Waleffe, Fabian 1997 On a self-sustaining process in shear flows. *Physics of Fluids* **9** (4), 883–900.

Zhou, Kemin, Salomon, Gregory & Wu, Eva 1999 Balanced realization and model reduction for unstable systems. *International Journal of Robust and Nonlinear Control* **9** (3), 183–198.